Journal of Solid State Chemistry 182 (2009) 1972–1981

Contents lists available at ScienceDirect

Journal of Solid State Chemistry

journal homepage: www.elsevier.com/locate/jssc

Structural, spectroscopic and magnetic investigation of the $LiFe_{1-x}Mn_xPO_4$ ($x = 0$–0.18) solid solution

Marcella Bini [a], Maria Cristina Mozzati [b], Pietro Galinetto [b], Doretta Capsoni [a], Stefania Ferrari [a], Marco S. Grandi [b], Vincenzo Massarotti [a,*]

[a] Department of Physical Chemistry "M. Rolla", University of Pavia, viale Taramelli 16, 27100 Pavia, Italy
[b] CNISM—Department of Physics "A. Volta", University of Pavia, via Bassi 6, 27100 Pavia, Italy

ARTICLE INFO

Article history:
Received 4 November 2008
Received in revised form
5 March 2009
Accepted 6 May 2009
In memoriam of Prof. C.B. Azzoni
Available online 19 May 2009

Keywords:
$LiFePO_4$
EPR
Magnetization
XRPD
Micro-Raman
Impurity phases
Cation distribution

ABSTRACT

Different solid state and sol–gel preparations of undoped and Mn substituted cathode material $LiFePO_4$ are investigated. Li_3PO_4, $Fe_2P_2O_7$ and $Li_4P_2O_7$ are detected and quantified by XRPD only in solid state synthesis. In addition, micro-Raman spectra reveal low amount of different iron oxides clusters. EPR data, combined with the results of magnetization measurements, evidence signals from Fe^{3+} ions in maghemite nanoclusters, and in $Li_3Fe_2(PO_4)_3$. The sol–gel synthesis, showing the lowest amount of impurity phases, seems the most suitable to obtain a promising cathode material. The structural refinement gives new insights into the cation distribution of the Mn doped triphylite structure: (i) about 85% of Mn^{2+} ions substitutes Fe^{2+}, the remaining 15% being located on the Li site, thus suggesting a structural disorder also confirmed by EPR and micro-Raman results; (ii) Mn ions on the Li site are responsible for the observed slight cell volume expansion.

1. Introduction

The $LiFePO_4$ (triphylite) compound finds application as cathode material in rechargeable lithium batteries [1–3]. It has the olivine crystal structure (space group *Pnmb*) [4] in which Li and Fe ions occupy two different octahedral sites and *P* ion the tetrahedral ones. High capacity (170 mA hg^{-1}) at moderate current densities, low toxicity and low cost [5] make it an ideal candidate to replace lithium manganese or cobalt oxides electrodes in lithium batteries. The low intrinsic electronic conductivity can be increased by mixing carbon additives to triphylite or by surface coating the $LiFePO_4$ particles by a thin carbon layer [6–8]. In addition, the presence of some impurity phases (e.g. Fe_xP or Fe_xN alloys, such as Fe_2P or Fe_2N and Fe_3N) that may form during the synthesis plays a favorable role in improving some electrochemical performances, in particular the conductivity value, even though in large quantities they worsen the cell capacity and cycling rate [9]. On the contrary, the poisoning of $LiFePO_4$ due to oxide-based impurity phases reduces the electrochemical performances. It is thus crucial to achieve a complete control of the formation and amount of impurity phases in order to obtain reproducible electrochemical properties, basic requirement for the large scale marketing of triphylite in the field of rechargeable batteries. In this frame a large number of synthesis routes, both solid state and sol–gel, for pure [10–12] and doped (Nb, Mg, Al, Zr or Ti on lithium site; Mn, Co, Ni on iron site) [13–15] triphylite, are reported in literature. The unwanted tendency of Fe^{2+} to oxidize to Fe^{3+} requires working in reducing or inert atmosphere. In some cases traces of phases containing oxidized iron, in particular iron oxides, can form (Fe_2O_3, as hematite or maghemite, or Fe_3O_4) probably as a consequence of the decomposition of the organic precursors used in the synthesis process. These phases strongly affect the magnetic properties of the material, showing themselves peculiar magnetic features that can help to determine their nature and, under certain circumstances, also their amount by means of magnetization or EPR measurements [16–20].

The aim of the present work is to compare $LiFePO_4$ different synthetic routes, in particular solid state and sol–gel synthesis, and to correlate them to the different impurity phases that can form. This purpose is reached by the combined use of X-ray powder diffraction (XRPD), electron paramagnetic resonance (EPR), magnetic and micro-Raman techniques. The main impurity phases are quantified by refining the XRPD patterns with the Rietveld method, while EPR, magnetization measurements and

* Corresponding author. Fax: +39 382 987575.
E-mail address: vincenzo.massarotti@unipv.it (V. Massarotti).

0022-4596/$ - see front matter © 2009 Elsevier Inc. All rights reserved.
doi:10.1016/j.jssc.2009.05.016

micro-Raman spectroscopy are accurately used to evidence the presence of different iron oxides or other phases whose abundance is under the XRPD detection limit.

Furthermore, Mn doped $LiFePO_4$ samples (3%, 9% and 18% of substitution on Fe site) were likewise synthesized and analyzed to investigate the role of doping on the impurity phases formation and on physical properties of the triphylite. In addition the Mn distribution on the cationic sites as well as the influence of Mn doping on triphylite structure was studied. Finally, the samples morphology and its dependence on the synthesis route and on doping were investigated by scanning electron microscopy (SEM).

2. Experimental

2.1. Synthesis procedures

The stoichiometric $LiFePO_4$ compound was synthesized following two solid state and one sol–gel route.

(1) A mixture of Li_2CO_3 (Sigma Aldrich 99+%), $NH_4H_2PO_4$ (Sigma Aldrich 99.99+%) and $Fe(CH_3COO)_2$ (Sigma Aldrich 99.995%) in the 1:2:2 stoichiometric ratio was weighted and stirred in acetone (Fluka 95+%) in a dry box apparatus until solvent evaporation is obtained. A 3% wt (SS1 sample) or 1.5% wt (SS2 sample) excess of Li_2CO_3 and $NH_4H_2PO_4$ was used to avoid lithium loss. The thermal treatment was performed in N_2 flow at 593 K for 3 h and 1073 K for 3 h with intermediate grindings.
(2) A stoichiometric mixture (1:2:2 ratio) of Li_2CO_3, $NH_4H_2PO_4$ and $FeC_2O_4 \cdot 2H_2O$ (Sigma Aldrich 99.99+%) was prepared and stirred in acetone (Fluka 95+%) in a dry box apparatus until solvent evaporation is obtained. The thermal treatment was performed in N_2 flow at 593 K for 1 h and for three times at 1073 K for 3 h with intermediate grindings (SS3 sample).
(3) Sol–gel synthesis [21]: a stoichiometric amount of $FeC_2O_4 \cdot 2H_2O$ and $LiNO_3$ (Sigma Aldrich 99.99+%) was dissolved in a 1 M nitric acid (Fluka 99+%) solution into which a citric acid solution (66% wt) was added drop-wise with continuous stirring. A 1:1 molar ratio between the citric acid (chelating agent) and the total metal ions was used. A saturated solution of $NH_4H_2PO_4$ (53% wt) was added and the mixture was gently heated with continuous stirring for 6 h to remove the excess water. The gel precursor was dried in a circulation oven at 333 K and treated at 723 for 2 h in N_2 flow (SG sample).

The Mn doped $LiFePO_4$ samples were prepared following the second synthesis route by adding $Mn(CH_3COO)_2 \cdot 4H_2O$ (Sigma Aldrich 99+%) in proper amount to obtain $LiFe_{1-x}Mn_xPO_4$ ($x = 0.03$, 0.09 and 0.18). In the following these samples will be named Mn3, Mn9 and Mn18.

2.2. Techniques

The X-ray powder diffraction patterns were collected on a Bruker D5005 diffractometer with a Cu$K\alpha$ ($K\alpha_1 = 1.5406$ Å; $K\alpha_2 = 1.5443$ Å) radiation in the angular range $15^\circ < 2\theta < 65^\circ$, step 0.015° and 0.5 s/step of counting time. A nickel filter and position sensitive detector (PSD) were used. The structural and profile refinement was performed on the diffraction patterns by means of Rietveld method (TOPAS 3.0 software) [22] to determine the main structural parameters, the Mn distribution between the Li and Fe octahedral sites and the weight percentage of the formed phases. The Mn occupancy factors were refined by allowing Mn to locate on both the cationic sites and by constraining the total Mn amount to the nominal content.

Scanning electron microscopy micrographs were collected on a Cambridge Stereoscan 200 microscope on gold sputtered samples at different magnifications. Moreover, EDS analysis was carried out on the Mn doped samples without Au sputtering.

EPR measurements were performed at about 9.4 GHz at room temperature (r.t.) with a Bruker spectrometer. Particular care was paid in determining the sample mass and position in the resonant cavity to compare signal intensities (areas) with those of suitable standards and to estimate the relative amount of the paramagnetic species in the samples. The derivative signal areas were computed by double integration with numerical methods.

Magnetization (M) measurements have been performed at 100 and 10 000 Oe from 352 to 2 K by means of a Squid magnetometer. M vs H curves have been also collected at different temperatures with magnetic field ranging between 0 and 30 000 Oe.

Micro-Raman measurements were carried out at r.t. by using a Labram Dilor spectrometer equipped with an Olympus microscope HS BX40. The 632.8 nm light from He–Ne laser was employed as excitation radiation. The samples, mounted on a motorized xy stage, were tested with a 100 × objective and with a laser spot of about 1 μm of diameter. The spectral resolution was about 1 cm^{-1}.

3. Results

3.1. XRPD

The XRPD patterns of the undoped $LiFePO_4$ samples are reported in Fig. 1: for the SS1, SS2 and SS3 samples, obtained via solid state route, the main diffraction peaks are those expected for the $LiFePO_4$ phase (JCPDS card no. 40-1499). However, weak peaks pertinent to impurity phases, such as Li_3PO_4, $Fe_2P_2O_7$ and $Li_4P_2O_7$, are present. Only the sol–gel route (SG sample) allows to obtain pure $LiFePO_4$ phase within the XRPD limit detection. The diffraction patterns of Mn doped $LiFePO_4$ are compared in Fig. 2: the undoped SS3 sample, obtained by the same synthesis route, is also shown. The patterns are typical of multiphase systems: $LiFePO_4$ is present together with small amount of Fe_3O_4 (inset of Fig. 2), $Fe_2P_2O_7$ and $Li_4P_2O_7$ impurity phases.

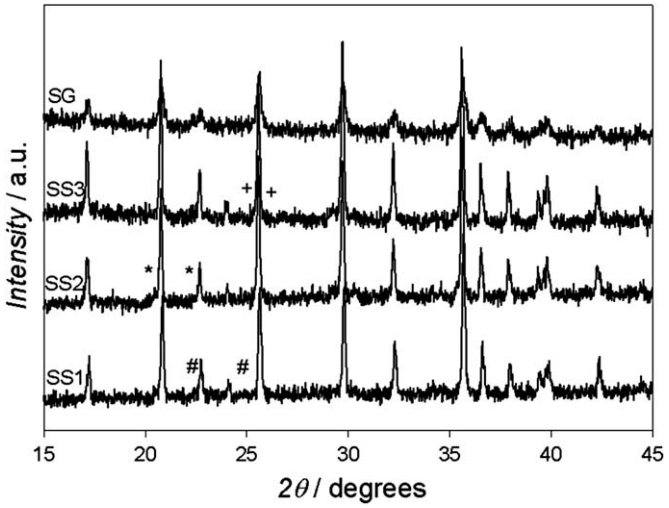

Fig. 1. XRPD patterns of undoped solid state and sol–gel $LiFePO_4$ samples. The main diffraction peaks of $Fe_2P_2O_7$ (+), Li_3PO_4 (#) and $Li_4P_2O_7$ (*) impurity phases are indicated.

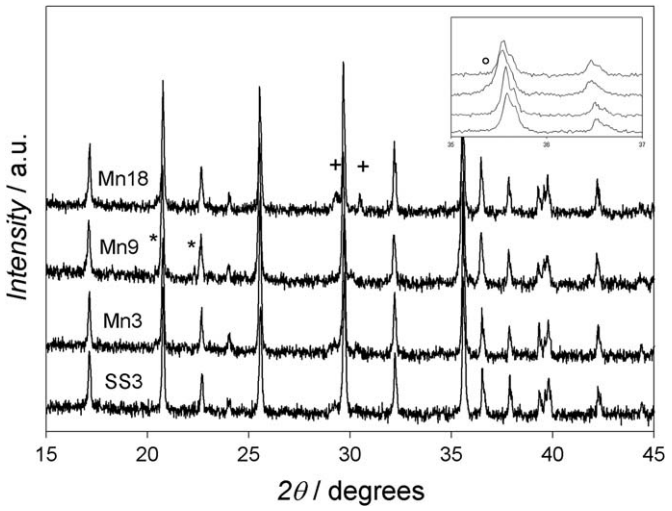

Fig. 2. XRPD patterns of Mn3, Mn9 and Mn18 doped samples together with the undoped one from the same synthesis (SS3). The main diffraction peaks of $Fe_2P_2O_7$ (+) and $Li_4P_2O_7$ (*) impurity phases are indicated. The inset evidences, in the Mn9 sample, the presence of the Fe_3O_4 phase (°).

Table 1
Lattice parameters, cell volume, isotropic thermal factors, mean Li–O and Fe–O bond length in LiO_6 and FeO_6 octahedra and compositional parameters for undoped samples, obtained from Rietveld refinement, together with the R_{wp} and GoF discrepancy factors.

Sample	SS1	SS2	SS3	SG
a (Å)	10.3266(7)	10.3259(5)	10.3255(5)	10.3243(27)
b (Å)	6.0068(4)	6.0048(3)	6.0035(3)	6.0057(16)
c (Å)	4.6905(4)	4.6891(3)	4.6879(3)	4.6942(16)
V (Å^3)	290.95	290.75	290.60	291.06
B(Li) (Å^2)	2.1(2.0)	0.2(1.7)	3.0(1.9)	4.0(3.7)
B(Fe) (Å^2)	1.0(3)	0.4(2)	1.9(3)	1.6(5)
⟨Li–O⟩ (Å)	2.10(2)	2.11(2)	2.14(3)	2.14(4)
⟨Fe–O⟩ (Å)	2.18(2)	2.16(2)	2.15(2)	2.17(2)
R_{wp}/GoF	2.43/1.09	2.25/1.05	2.13/1.08	1.98/1.00
%wt $Li_4P_2O_7$	2.8(6)	3.7(6)	–	–
%wt Li_3PO_4	3.1(8)	–	–	–
%wt $Fe_2P_2O_7$		7.2(7)	5.8(7)	–

In Tables 1 and 2 structural and compositional parameters and the R_{wp} and GoF discrepancy factors obtained from the Rietveld refinement are reported for the undoped and Mn doped $LiFePO_4$ samples, respectively. The isotropic thermal factors (*B*) of Li and Fe sites are positive, as well as those of *P* and *O* ones (values ranging between 0 and 3 Å^2), not reported in Tables 1 and 2 for sake of simplicity. Interesting results are obtained by the occupancy factors refinement (Table 2): for all the doped samples the presence of Mn on the lithium site is suggested. The refined Mn amount on this site increases on increasing the Mn content in the synthesis, and represents the 13.3% for the Mn3 and Mn9 samples and 15.5% for the Mn18 one. The refined atomic fractional coordinates are in really good agreement with the literature ones [4]; attention was paid to the Li–O and Fe–O bond lengths in the LiO_6 and FeO_6 octahedra: the mean bond distance for each sample is reported in Tables 1 and 2. On the whole, the results obtained by Rietveld refinement are satisfactory, as suggested also by the reliable values of the discrepancy factors R_{wp} and GoF.

3.2. SEM

In Fig. 3, as an example, the SEM micrographs of SS3 (a), Mn3 (b), Mn9 (c) and SG (d) samples are shown. Wide agglomerates

Table 2
Lattice parameters, cell volume, isotropic thermal factors, occupancy factors on Li and Fe sites, mean Li–O and Fe–O bond length in LiO_6 and FeO_6 octahedra and compositional parameters for Mn doped samples, obtained from Rietveld refinement, together with the R_{wp} and GoF discrepancy factors.

Sample	Mn3	Mn9	Mn18
a (Å)	10.3276(4)	10.3345(5)	10.3515(4)
b (Å)	6.0062(2)	6.0125(3)	6.0233(3)
c (Å)	4.6892(2)	4.6936(3)	4.7007(2)
V (Å^3)	290.87	291.64	293.09
B(Li) (Å^2)	2.5(1.5)	3.0(2.1)	1.7(1.1)
B(Fe) (Å^2)	1.8(2)	1.5(2)	1.5(3)
N:Li	0.996(4)	0.988(8)	0.972(4)
Mn	0.004(4)	0.012(8)	0.028(4)
N:Fe	0.974(4)	0.922(8)	0.848(4)
Mn	0.026(4)	0.078(8)	0.152(4)
⟨Li–O⟩ (Å)	2.10(2)	2.14(1)	2.17(1)
⟨Fe–O⟩ (Å)	2.17(2)	2.16(2)	2.15(2)
R_{wp}/GoF	2.21/1.07	2.06/1.05	2.38/1.07
%wt $Fe_2P_2O_7$	7.1(6)	1.9(5)	5.9(4)
%wt $Li_4P_2O_7$	1.4(4)	1.2(4)	–
%wt FeO	–	0.6(3)	–
%wt Fe_3O_4	–	2.7(6)	–

(about 40 μm) of undefined shape of joined squared particles are evident in SS samples (Fig. 3a–c); the doping does not seem to influence the samples morphology, which is comparable to that of the undoped one. On the contrary, the sol–gel sample (Fig. 3d) shows agglomerates (1–2 μm) formed by small distinct rounded particles. EDS analysis, carried out on the Mn doped samples, shows homogeneous distribution of Mn ions in the crystalline powders.

3.3. EPR

The r.t. EPR spectra of the undoped samples (SS1, SS2, SS3 and SG) are reported in Fig. 4a. Two main components may be clearly observed for all the samples: a narrow signal centered at about 3370 G ($g \cong 2$) and a broad signal centered at lower resonant magnetic fields. Analogous picture concerns the Mn3 and Mn18 doped samples, whose r.t. EPR spectrum is shown and compared to the SS3 undoped one in Fig. 4b. The EPR signal of Mn9 sample, shown in the inset of the same figure, is strongly affected by the presence of a remarkable amount of the Fe_3O_4 impurity phase (see Table 2), already observed in other Fe-based compounds [23].

3.4. Magnetization

The temperature dependence of the magnetization has evidenced that both undoped and Mn-doped samples undergo the paramagnetic to antiferromagnetic transition with Néel temperature (T_N) of about 50 K, typically observed for the pure $LiFePO_4$ compound [9,16,20,24–28]. In Fig. 5a the *M*/*H* vs *T* curve, obtained applying a 10 000 Oe magnetic field, is reported for the SS3 and the Mn3 samples. The inverse of these curves is also shown (inset a). At least two features deserve to be pointed out. First, a sharp increase in the *M*/*H* vs *T* curves occurs below 30 K, as well evidenced by the curve recorded at 100 Oe for the SS3 sample (inset b), suggesting the presence of a ferromagnetic-like impurity with Curie Temperature (T_C) near 30 K. The antiferromagnetic behavior at about 15 K, more evident for the Mn-doped sample, is instead due to the presence of the $Fe_2P_2O_7$ phase [29], well detected by XRPD (Table 2). Secondly, deviation from the expected linear behavior occurs in the *H*/*M* curves (see inset a), even at temperatures far enough from T_N, suggesting the presence, up to the highest investigated temperatures, of an additive "saturated" *M* contribution. This contribution, which prevents us to extract

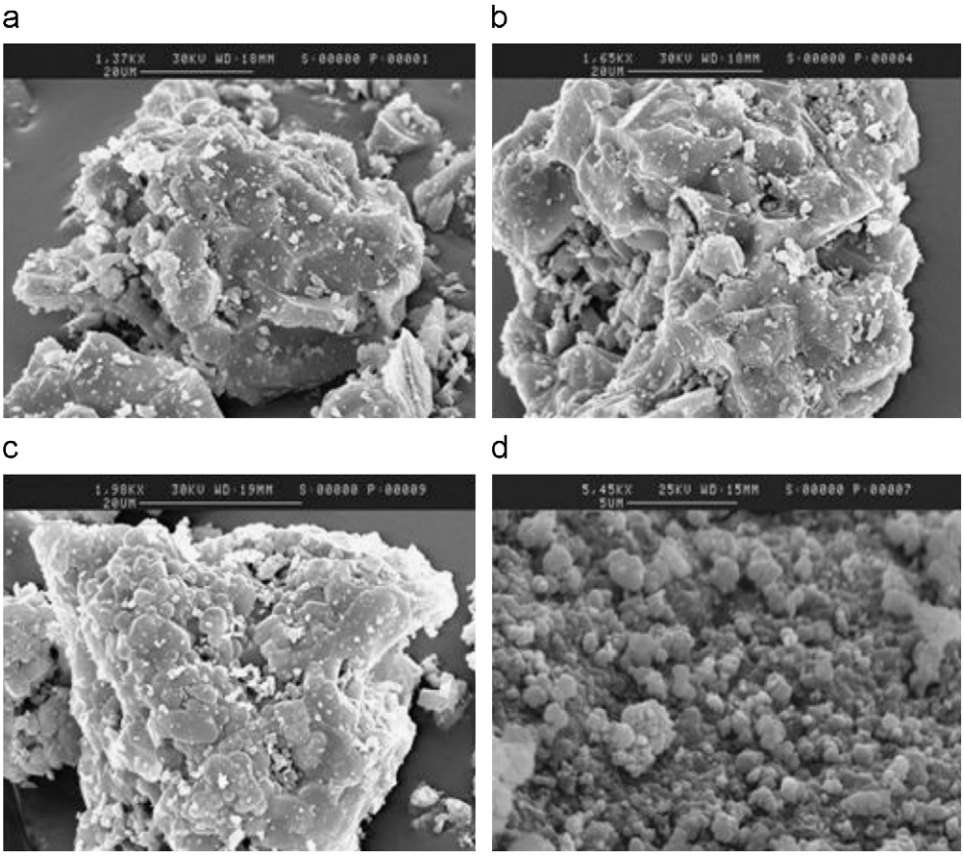

Fig. 3. SEM micrographs of (a) SS3, (b) Mn3, (c) Mn9 and (d) SG samples.

the Curie–Weiss parameters from the H/M curves, is ascribable to a ferromagnetic-like phase with transition temperature outside the investigated temperature range, probably nano-clusters of Fe-based compounds, often found in these materials [9,16,20,24,26]. M vs H measurements performed at different temperatures provide information on nature and features of these magnetic impurities. The results obtained in the temperature range 100–300 K for the two representative samples are reported in Fig. 5b.

3.5. Micro-Raman

The spatial resolution of the laser spot allowed us to perform the Raman mapping from extended region of each sample obtaining "average" spectra, representative of the main phases of each sample, and "peculiar" spectra, due to impurity phases present in low quantity only in some regions of the samples. In Fig. 6 we report the "average" Raman spectra recorded at r.t. for all the samples, except for the SG, shown in the inset. We can observe in all cases common main spectral features: the most intense Raman signals are observed in the region 900–1200 cm^{-1}, while several weaker peaks are present at lower frequencies. The Raman modes are due to the vibrations of $LiFePO_4$ lattice that can be qualitatively seen as divided into two classes, i.e. internal and external modes with respect to the PO_4^{3-} vibrational unit. The internal modes are due to intramolecular vibrations of PO_4^{3-} ions, with a correlation between the motions of the phosphate anions inside the unit cell. The resulting Raman spectrum is thus dominated by the stretching and bending modes of the PO_4^{3-} ions, being the first located in the high energy part of the spectrum and the most intense as usual. The motion of Li ions gives very weak contributions to these vibrations. The optical external modes, due to proper vibrations of the whole lattice, observable at lower energies around 400 cm^{-1}, are mainly due to translational motions of PO_4^{3-} and Fe^{2+} ions [9].

In the "average" Raman spectrum of SS pure $LiFePO_4$ compound (Fig. 6) the strongest signal is peaked at ~954 cm^{-1} and is due to symmetric stretching mode v_1, while the two bands at ~999 and 1070 cm^{-1}, respectively, are due to antisymmetric stretching v_3. The bending modes give rise to the three observed modes at 575, 594 and 633 cm^{-1}, while the broadened structure at ~440 cm^{-1} could be due to the overlapping of different bending modes. Below 400 cm^{-1}, the external optical modes are observed. Different features must be nevertheless pointed out for the Mn9 sample, whose spectrum is instead characterized by decreasing of Raman signals at higher energies and a broadened scattering extending all over the 200–800 cm^{-1} range.

The SG spectrum extends up to 2200 cm^{-1} (inset of Fig. 6) due to the presence of intense Raman modes at 1325 and 1580 cm^{-1} not observed in the other samples. These strong signals are very well known and ascribable to the presence of the graphitic carbon layer covering the triphylite particles [20] derived from the preparation method.

In Fig. 7, as an example, we report the "peculiar" spectra of the SS3 sample (traces b–d) together with its average spectrum (trace a) and the spectrum of sol–gel sample (trace e). Several differences can be observed among these spectra: the main spectral modifications are in the region 650–800 cm^{-1}, around 1050 cm^{-1} and at lower frequencies, below 400 cm^{-1}. In particular, the spectrum b is characterized by a broad band at ~660 cm^{-1}, completely different from the features of spectrum a in the same energy region. In addition, in spectrum b we observe a net decrease of the Raman scattering of the stretching modes

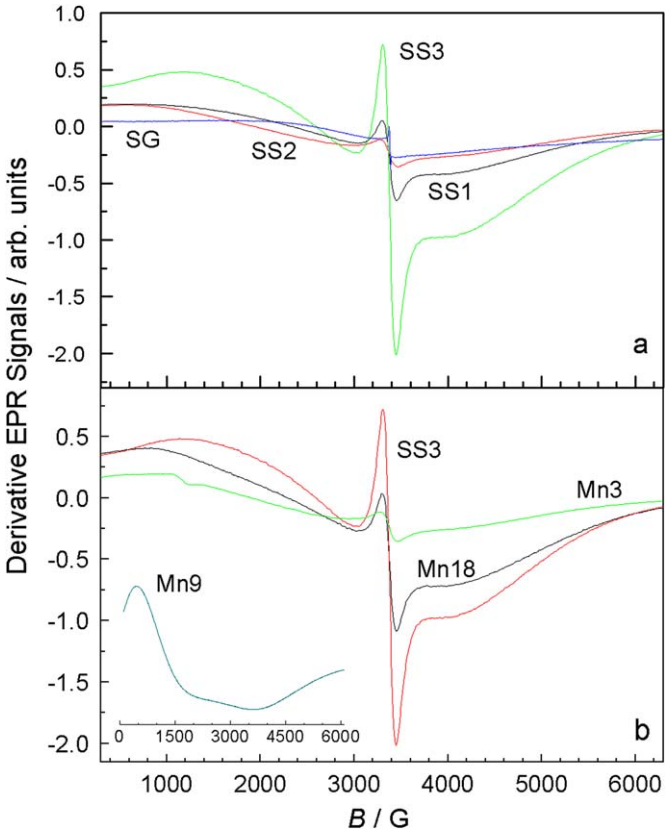

Fig. 4. (a) EPR spectra of undoped $LiFePO_4$ samples. (b) EPR spectra of Mn doped $LiFePO_4$ samples (Mn9 signal is reported in the inset) compared to the undoped SS3 one.

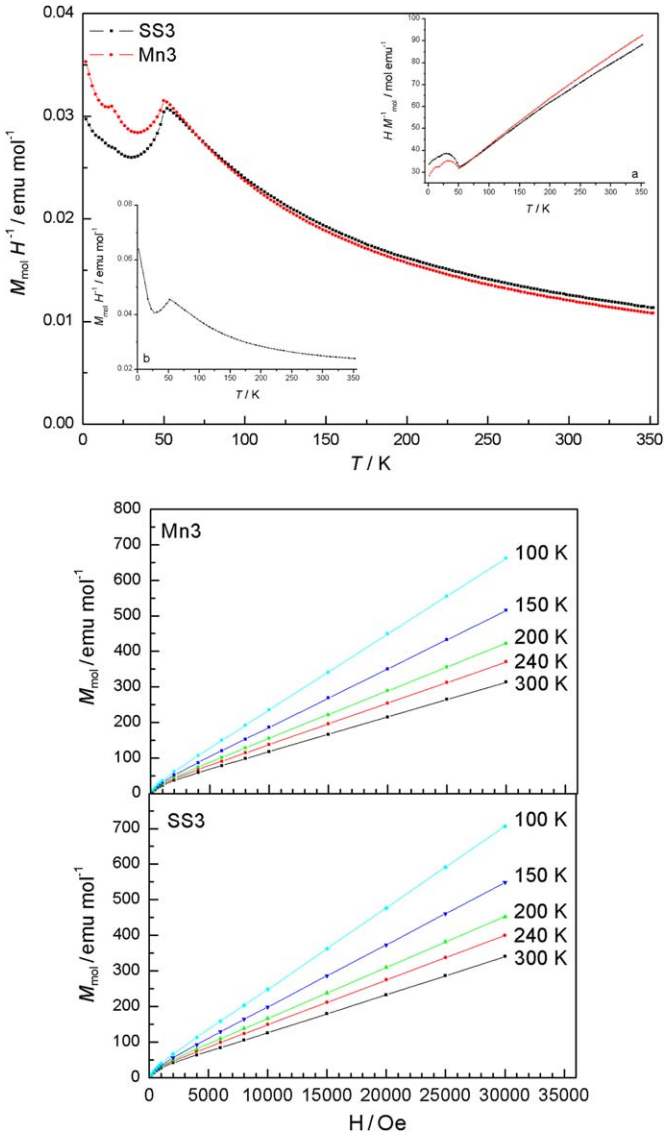

Fig. 5. (a) M_{mol}/H vs T curves of SS3 and Mn3 samples, obtained applying a 10 000 Oe magnetic field. In the inset a the H/M_{mol} vs T curves at 10 000 Oe for the same samples are reported, while in the inset b the M_{mol}/H vs T curve for the SS3 sample recorded at 100 Oe is shown; (b) M_{mol} vs H measurements at different temperatures for the SS3 and Mn3 samples.

around 1000 cm^{-1}. In spectrum *c*, these modes are practically absent and we observe the appearance of intense mode at ~1040 cm^{-1} accompanied by a broadened shoulder at higher energies. Also at lower frequencies the spectrum *c* appears completely different from spectrum *a* and no spectral coincidences can be observed. Less intense modes are detected at 710, 520, 280 and 220 cm^{-1}. In spectrum *d* we can notice the presence of the "usual" signals from olivine structure with the simultaneous presence of two overlapping bands centered at 660 and 710 cm^{-1}, respectively. Finally in spectrum *e* (SG sample), the intense Raman bands from olivine cages are absent while signals at 210, 275 and 400 cm^{-1} can be detected.

4. Discussion

It is well known from literature that the synthesis of triphylite as a single phase is quite difficult, independently of the kind of synthesis route, due to the strong tendency of iron to oxidize to +3 oxidation state [16,27]. The control of the formation of different impurity phases requires combining structural, electronic and magnetic properties characterization thus overcoming the limits of a single technique in the impurities detection.

In this frame, the sol–gel synthesis seems to be more promising in obtaining a good compromise between crystalline quality and high purity level. From SEM images, the SG sample shows a morphology characterized by small rounded particles forming agglomerates. This observation agrees with the less crystallinity degree evidenced by XRPD pattern (Fig. 1, SG), showing broad diffraction peaks typical of small particle samples: crystallite size values of 40 nm are determined from Rietveld refinement. The low crystallinity, justified by the low temperature of thermal treatment of SG sample with respect to the SS ones, is also supported by Raman results. In fact, the main peaks ascribable to stretching vibrations of PO_4 units are strongly depressed, denoting a significant disorder. In addition, the main features of the SG spectrum are due to a residual of carbon layer after the synthesis procedure as previously well evidenced [9]. Indeed, the structures at 1583 and 1345 cm^{-1} correspond, respectively, to the *G* line, associated with the optically allowed E_{2g} zone center mode of crystalline graphite, and to the *D* line, associated with disorder-allowed zone-edge modes of graphite not detectable by XRPD and EPR. These broadened spectral features indicate that a highly amorphous carbon film is deposited on the triphylite grains. Moreover, only in the Raman spectrum we can clearly recognize the presence of hematite particles, instead not evidenced in the EPR spectrum. This fact seems, at a first sight, contradictory but really it suggests that the hematite clusters could be formed under laser irradiation [37].

The results for SS undoped and doped samples appear rather different from the SG ones. Indeed, the diffraction patterns of solid

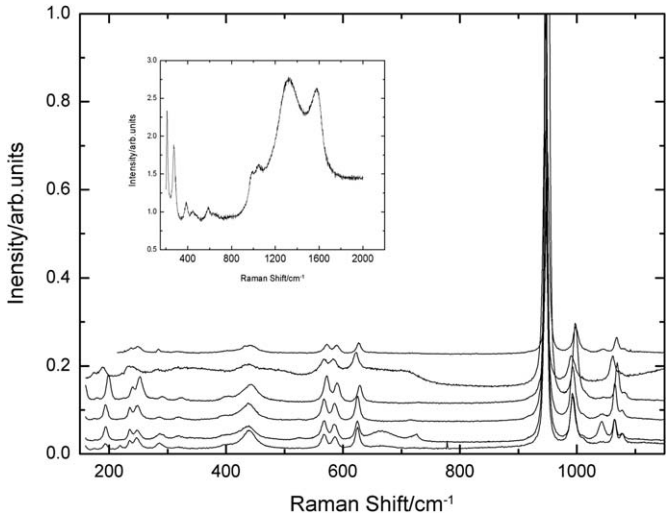

Fig. 6. "Average" r.t. Raman spectra of all the SS investigated samples: SS1, SS2, SS3, Mn3, Mn9 and Mn18, starting from the bottom. In the inset the Raman spectrum of SG sample is reported on an extended range.

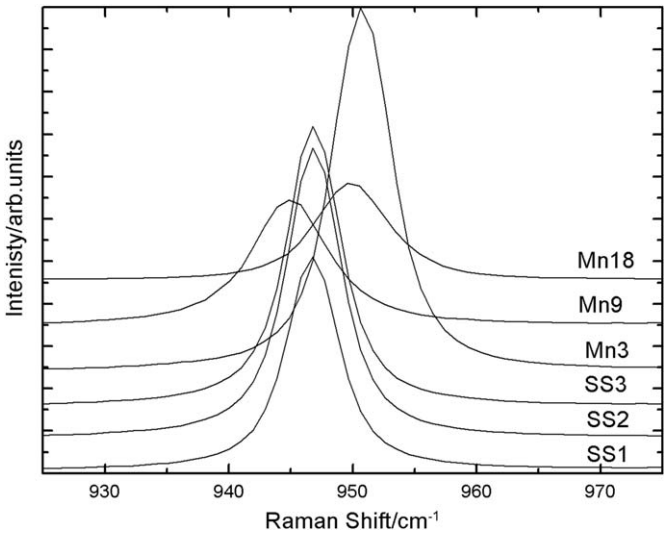

Fig. 8. Detailed region of Raman stretching mode of PO_4 cage for all the investigated samples.

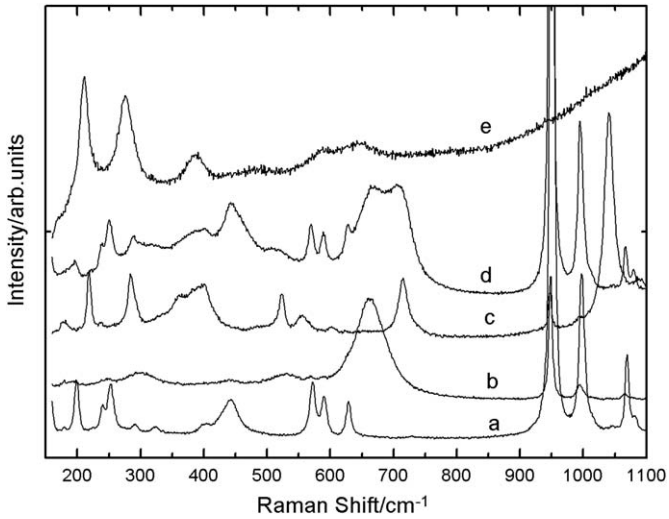

Fig. 7. "Peculiar" r.t. Raman spectra of SS3 (traces *b–d*) compared to the average spectrum of the same sample (trace *a*) and to the SG sample spectrum (trace *e*).

state samples (Figs. 1 and 2) show, together with the main triphylite component, the presence of $Fe_2P_2O_7$, Li_3PO_4 and $Li_4P_2O_7$ phases.

The SEM images of SS samples (Fig. 3a–c) show similar morphology and wide particles agglomerates, with squared and irregular shape, formed by small particles jointed together. These micrographs suggest a high level of sinterization and a possible partial fusion process is evidenced by their glazed aspect. From Rietveld refinement, in fact, we determine a crystallite size value of 125 nm, thus larger than that of the SG sample.

Concerning the Raman results, the "average" spectra reported in Fig. 6 are in agreement with both theoretical and experimental works devoted to the study of $LiFePO_4$ Raman scattering [9,30,31], with the strongest Raman modes peaked in the high energy region of the spectrum. These features are common to all the SS samples, notwithstanding the differences previously pointed out for Mn9. From a detailed analysis of the main Raman peaks due to symmetric stretching in PO_4 cage (Fig. 8), we can deduce some information on the crystalline order. The symmetric shape of this mode can be analyzed with a best-fitting procedure using a Lorentzian curve as a fitting function. The energy of this mode is the same for all the undoped samples, while small changes are seen in Mn doped ones even if without a clear correlation with the Mn amount. On the contrary, the full width at half maximum (FWHM) parameter shows a significant increase in doped samples (from 4.9 cm^{-1} for undoped samples to 5.4, 7.5 and 6.6 cm^{-1} for Mn3, Mn9 and Mn18 samples, respectively). These parameters indicate that the insertion of Mn tends to disturb the vibrations of PO_4 cages and in particular Mn9 is characterized by a higher degree of disorder. Direct influences of Mn substitution should be evidenced in the low energy part of the spectrum where the vibrations involving Fe^{2+} and Li^+ ions should appear. From Fig. 6, we can notice that for more substituted Mn samples (Mn9, Mn18) just in this part of the spectra, Raman signals are different with respect to those of pure samples but the complex shape of the bands due to the presence of several overlapping peaks with different origin hinders a more detailed analysis. In any case, these results are supported by EDS analysis, showing a homogeneous distribution of the Mn ions in the samples, and by the lattice parameters increasing on the increase in the Mn amount (Table 2), indicating that the Mn substitution on cationic sites really takes place. In fact, the ionic radius of Mn^{2+} in octahedral coordination (0.83 Å) is slightly higher than that of Fe^{2+} (0.78 Å) and of Li^+ (0.76 Å) [32] in the same coordination and a slight cell volume expansion is expected, according to Vegard's law. Some interesting consideration can be made on the mean Li–O and Fe–O bond distances in the LiO_6 and FeO_6 octahedra (Tables 1 and 2), calculated from the refined fractional atomic coordinates. While a slight expansion is observed for the LiO_6 octahedron, which passes from 2.12 Å (mean value for the SS undoped samples) to 2.17 Å (Mn18), an approximately constant value is instead observed for the FeO_6 octahedron. This suggests that the slight increase of the lattice parameters (about 0.25%) and the cell volume (about 0.7%) observed by increasing the nominal Mn content could be substantially attributed only to about 15% of Mn ions present on the lithium site. The substitution of Li^+ ions with the aliovalent Mn^{2+} ions requires the formation of defects in the triphylite structure; for example, cationic vacancies should be taken into account for charge balancing. Li vacancies formation can be mainly considered due to the low X-ray scattering power of Li ions.

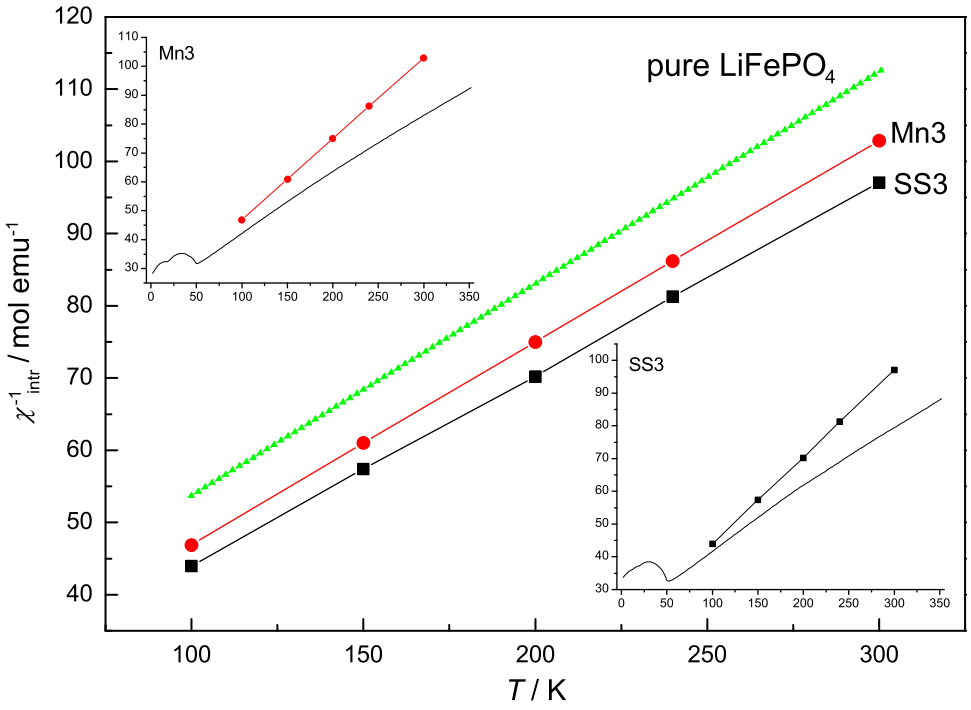

Fig. 9. $1/\chi_{intr}$ (obtained from the linear behavior of M_{mol} vs H curves) of SS3 and Mn3 samples compared to the $1/\chi$ curve of pure $LiFePO_4$ derived from literature [20]. In the insets, the same $1/\chi_{intr}$ curves for SS3 and Mn3 samples are compared to the corresponding H/M_{mol} vs T curves.

As previously mentioned, XRPD revealed different phases in all the SS samples. In particular in the Mn9 sample also the magnetite phase is present (inset of Fig. 2), as confirmed by the form of the related EPR signal (inset of Fig. 4b). We point out that the main peaks of hematite (33.2°), goethite (21.2° and 36.7°) and wustite (41.7°) could be easily detected (background region for $LiFePO_4$), whilst the main diffraction peak of the maghemite phase (about 35.6°) completely overlaps with those of triphylite. However, the presence of other iron oxides in quantities below the detectable limit of XRPD technique cannot be ruled out. It is thus important to derive additional information from the Raman spectra of "peculiar" points. The "peculiar" spectra of the SS3 sample reported in Fig. 7, for example, give evidence of the presence of Raman signals not pertinent to the typical spectrum of olivine structure (spectrum *a*). In particular spectrum *b* is mainly characterized by a strong signal around 662 cm^{-1} and weak structures at lower frequencies. In this spectrum the fingerprint of the Raman signals of Fe_3O_4 magnetite particles is recognizable [33]. Spectrum *c* denotes a strong decrease of stretching modes of $LiFePO_4$ and an intense mode at 1044 cm^{-1} with a broadened shoulder at higher energies. All the features of this spectrum are compatible with the spectrum of $Fe_2P_2O_7$ compound [34], also evidenced by XRPD and magnetic measurements. The strongest signals of the spectrum *d* are due to stretching vibrations of PO_4 units in $LiFePO_4$ structure but it is interesting to observe the region around 700 cm^{-1}: two overlapping structures at 660 and 710 cm^{-1} are observed. At lower frequencies other spectral changes are observed. This spectrum is the result of Raman scattering from clusters with a mixture of olivine and maghemite structures [33].

From Raman results it is difficult to obtain quantitative information about the abundance of a specific impurity phase inside the host matrix due to the fact that the technique has a spatial resolution of 1 μm and the scattered yield depends on several factors, like the morphology and the phase homogeneity across the sample. A more complete characterization of impurity phases can be obtained combining and correlating the structural characterization with the study of the magnetic properties of the samples. Indeed, the magnetic investigation has been found to be a powerful tool to verify the presence of magnetic impurity phases, in particular in form of nano-sized clusters, and to characterize their nature, concentration, average size and magnetic features. Both strongly magnetic γ-Fe_2O_3 (maghemite) and weakly magnetic Fe_2P (barringerite) clusters have been detected in many cases in $LiFePO_4$ samples [9,16,20,24,26], their resulting formation strictly related to the preparation method [9,16]. In addition, for Mn doped samples, the analysis of dependence of the magnetization on temperature and magnetic field can help in detecting possible effects of Mn doping on the intrinsic physical properties of the $LiFePO_4$ phase.

The overall features of the magnetization are similar for undoped and Mn-doped samples. In particular, by looking at the magnetic field dependence at different temperatures (Fig. 5b), a nonlinear M vs H behavior at low magnetic fields is observed for all the temperatures, followed by a strictly linear behavior at higher magnetic fields. The trend of these curves strongly resembles those already observed for the $LiFePO_4$ compound in the presence of γ-Fe_2O_3 nano-clusters [9,16,20,24,26], whose T_C is much higher than r.t. ($T_C = 858$ K) [35]. In particular, while the linear M vs H behavior should represent the "intrinsic" $LiFePO_4$ contribution to M, the nonlinear one should come from the "extrinsic" maghemite contribution. So, also in our undoped and Mn-doped samples, the nature of the "saturated" magnetic contribution inferred from the M temperature dependence is most likely ascribable to the maghemite, whose presence has been directly evidenced by Raman spectra and which, moreover, quite easily tends to form nanoparticles in iron compounds [16,24]. On the other hand, the presence of Fe_2P nano-clusters, which can be themselves responsible for magnetic extrinsic contribution in these compounds, is ruled out from the absence of magnetic transition in the M/H vs T curves in the range 210–260 K [16,20,26].

A value of saturation magnetization (M_S) roughly independent of the temperature is obtained when the linear behavior (occurring for $H \geq 4000$ Oe) is extrapolated to $H = 0$, further supporting the hypothesis that the magnetic clusters are constituted by maghemite. From this value, due to the whole maghemite amount in the sample, a concentration of about 0.2% (SS3 sample) or even lower (0.18% for Mn3 sample) is obtained for the γ-Fe_2O_3 phase, consistently with what reported in literature (e.g. 0.18% of maghemite had been detected in carbon free samples [9]). Clearly, the γ-Fe_2O_3 amount is not detectable by X-ray diffraction, due to the low quantity of this phase and to the large peak overlapping of diffraction peaks of maghemite with those of triphylite. A negligible amount of γ-Fe_2O_3 magnetic clusters can be inferred also for the SG sample, as supported by the EPR data (see later).

Following the procedure commonly reported in literature [9,16,20,24,26], we tried to analyze the "extrinsic" contribution of the maghemite in our M vs H curves in the frame of the superparamagnetic model, supposing that no magnetic interaction occurs between the ferrimagnetic clusters. Besides, a negligible interaction between magnetic clusters and $LiFePO_4$ matrix is supposed by adding the "intrinsic" contribution $\chi_{intr} \cdot H$ due, in principle, only to the pure triphylite phase.

Our M vs H curves are well computed by the function

$$M = \chi_{intr} \cdot H + M_S \cdot L\left(\frac{n\mu H}{k_B T}\right)$$

where $L(n\mu H/k_B T)$ is the Langevin function, well suitable to describe the superparamagnetic behavior [9,16,20,24,26].

The saturation magnetization is usually written as

$$M_S = Nn\mu$$

where μ can be considered the saturation magnetic moment of the single γ-Fe_2O_3 particle ($\mu = (10/3)\mu_B$) [9,20], n is the average number of γ-Fe_2O_3 particles in one cluster (the clusters size dispersion has not been taken into account in the Langevin function) and N is the number of maghemite clusters in the sample. The computation of the magnetization with the above equation allowed us to estimate the average size of the magnetic clusters and their concentration: values between 2200 and 2500 have been obtained for n, while the N values correspond to about 0.5 ppm, i.e., on average, 0.5×10^{-6} N_A clusters per mole of $LiFePO_4$. These n and N values fairly agree with those reported in literature for single-domain nano-clusters (related to the n value) with a noncollective behavior (as deduced from the very low N values) [9,16,26], in full agreement with the considered model of superparamagnetism.

From the above analysis no substantial difference concerning the formation and characteristics of magnetic nano-clusters can be determined as a consequence of the Mn/Fe substitution, confirming that this feature is strictly related to the synthesis procedure. Rather, a not negligible effect of the Mn/Fe substitution can be expected on the intrinsic properties of the triphylite phase. For this purpose, we calculated the χ_{intr} values from the linear behavior of the M vs H curves at the different temperatures (between 100 and 300 K) and reported them, for the two representative samples, in Fig. 9 as $1/\chi_{intr}$, together with the $1/\chi$ curve of the pure $LiFePO_4$ deduced from literature data [20]. In the insets of the same figure, the $1/\chi_{intr}$ curves for the two samples are compared to the corresponding H/M vs T curve. The difference between $1/\chi_{intr}$ and H/M curves again evidences the presence in the samples of the "saturated" additive contribution due to the magnetic nano-clusters coexisting with the triphylite phase. Besides, the linear dependence with T of $1/\chi_{intr}$ is clear-cut so that we can now estimate the values of the Curie–Weiss constants, C_{mol} and θ. The C_{mol} value obtained for the SS3 sample is appreciably higher than the one of pure triphylite [20], as evidenced from the different slopes of the two $1/\chi$ curves, and it corresponds to an effective magnetic moment value of $5.50\mu_B$. This high value is consistent with the presence, in the sample, of paramagnetic impurities, as also already observed by other authors [27]. In our case, for example, a not negligible amount of $Fe_2P_2O_7$, purely paramagnetic in the considered temperature range [29], has been well evidenced also by XRPD data in all the SS samples (Tables 1 and 2), as well as by the presence of its characteristic modes in the Raman spectrum. Besides, low amount of paramagnetic phases evidenced from the EPR results ($Li_2Fe_3(PO_4)_3$, see later) contribute towards enhancing the C_{mol} value, in particular for the SS3 sample. The lowest $|\theta|$ value (θ is negative, indicating an antiferromagnetic coupling between spins) with respect to the pure triphylite phase suggests a weakening of the antiferromagnetic interactions. This is not surprising because the antiferromagnetic order can be easily locally destroyed by various kinds of defects or impurities due to the characteristic frustration of the triphylite phase [16].

The Mn addition lowers, as well, the $|\theta|$ value with respect to the pure compound [20], for reasons similar to those invoked for the SS3 sample. Besides, the C_{mol} value results to be higher than the one of pure $LiFePO_4$ and lower with respect to the SS3 sample (compare the slopes of the three $1/\chi$ curves). The trend of C_{mol} values is consistent with both the Mn^{2+} magnetic moment value, higher than for Fe^{2+}, and the amount of paramagnetic and diamagnetic impurity phases in the samples. Nevertheless the extent of the C_{mol} lowering in the Mn substituted sample with respect to SS3 is much greater than expected so that other features must be accounted for.

Indeed, we have to consider that Mn ions should be distributed in the $LiFePO_4$ structure, according to the increase of the lattice parameters with increasing Mn substitution and according to the Mn occupancy factor refinement on the Li and Fe sites, as previously pointed out. So, we can suppose that, in addition to the presence of different impurity phases that already entail the C_{mol} lowering with respect to the SS3 sample, Mn ions could create regions of $LiMnPO_4$, isomorphic to $LiFePO_4$ but with lower C_{mol} and θ values [25]. Likewise, the Mn substitution could favor the formation of small delithiated regions in the triphylite phase which could locally induce the formation of Fe^{3+} ions, possibly at the surface of the $LiFePO_4$ particles, where the Fe^{3+} ions could even change their spin state from high spin ($S = 5/2$) to low spin ($S = 1/2$), as found, for example, for small $LiFePO_4$ particles [36]. A paramagnetic contribution for $T \to 0$, possibly consistent with the presence of these Fe^{3+} ions, is indeed evident in the M vs T curve of Mn3 sample (Fig. 5a). This agrees with the fact that Raman spectroscopy more easily evidences regions with Fe^{3+} impurity phases in Mn doped samples.

Concerning the EPR measurements we should remember that in the pure $LiFePO_4$ triphylite phase, the Fe ion is present in the 2+ oxidation state only. For this d^6 ion no EPR signal is expected, due to the strong coupling with the lattice by the crystal field (Fe^{2+} has orbital momentum $L = 2$), which leads to a broadening of the related signal [16,23]. This has been indeed experimentally verified for pure $LiFePO_4$ [25]. As a consequence, the two signal components detected in our samples should be attributed to different Fe^{3+}-containing "phases".

The narrow signal centered at $g \cong 2$ shows, for all the SS samples, the same line shape, Lorentzian, and line width ($\Delta B \cong 140$ G), but different intensities, so that it can be attributed to different amount, in the different samples, of the same spurious phase containing Fe^{3+} ions, in a fully paramagnetic regime. For the SS3 sample, a Fe^{3+} ($S = 5/2$) paramagnetic center density as high as $7.6 \times 10^{19}\,g^{-1}$ has been estimated after double integration of this signal and comparison with a standard reference sample.

Table 3
$Li_3Fe_2(PO_4)_3$ amount determined by EPR measurements.

Sample	% mol $Li_3Fe_2(PO_4)_3$
SS1	0.27
SS2	0.15
SS3	1.00
SG	$\sim 2 \times 10^{-3}$
Mn3	0.15
Mn18	0.40

Some suggestions concerning the origin of this narrow EPR signal can be deduced from the temperature dependence of the magnetization. Indeed, the quite sharp increase of M at about 26 K, also observed in other $LiFePO_4$ samples [20,27], suggests the presence of the $Li_3Fe_2(PO_4)_3$ phase, which, both in rhombohedral and in monoclinic forms, exhibits a magnetic transition from a paramagnetic to a weakly ferrimagnetic phase at 27 or 29 K, respectively [19,36]. Moreover, the EPR signal at r.t. reported for the monoclinic $Li_3Fe_2(PO_4)_3$ [19] has analogous line shape and line width of the narrow signal detected in our samples. So, from the value of paramagnetic center density obtained above, it can be deduced that about 1 mol% of the $Li_3Fe_2(PO_4)_3$ phase is present in the SS3 sample. Since the shape of the narrow signal is the same, it is easy to estimate the percentage of this phase in all the samples from the simple ratio of the intensities, taking into account the samples masses. These values, reported in Table 3, are all lower than 1 mol%, explaining why this phase is hardly detectable from the XRPD. For the SG sample, a negligible paramagnetic center density ($\sim$20 ppm), whichever is its origin, is related to the much narrower ($\Delta B \cong 9$ G) Lorentzian signal component centered at $g \cong 2$.

The broad EPR component shows a more complex line shape, different for different samples, generally centered at lower resonant magnetic fields. As suggested by the results of magnetization measurements, this signal is attributable to the very low concentration of nanometer-sized maghemite clusters, with very large magnetic moment. For not interacting particles, a signal centered at $g \sim 2$ should be indeed expected. Nevertheless, different and complex signal shapes are reported in literature for these signals [16,24] and a clear understanding is still lacking.

In our case, the broad line shape can come from an overall disorder induced by the presence of magnetic impurities, in addition to the nano-sized clusters. The Fe ions in these impurities, with different crystal field parameters, can indeed play a role in the broadening of the spectra. Besides, the presence of Mn ions on both Fe and Li sites and the possible presence of small amount of Fe^{3+} with different spin state are potentially a further source of disorder and so a further reason for the line broadening: the broader line shape is indeed observed for the Mn18 sample.

From the EPR data, comparable values of the maghemite amount can be deduced for all the SS samples while the SG sample, also in this case, shows the narrower and less intense signal, corresponding to a negligible maghemite amount. We point out that, in principle, such signal could arise from different kinds of clusters (the sol–gel synthesis seems to favor the formation of Fe_2P clusters [27], even if in our case this hypothesis has been ruled out from magnetization measurements) or from residual impurities or defects, as Fe^{3+} ions associated to lithium vacancies, defects which are easily affected by their local surroundings [9].

At first glance some contradictions could appear comparing EPR and Raman results, but, as already mentioned about the presence of hematite in the Raman spectrum of SG sample, we have to take into account also the thermal instability of the different iron oxides. Indeed under laser irradiation, the thermal effect of light can induce the following transformation: $Fe_3O_4 \rightarrow \gamma - Fe_2O_3 \rightarrow \alpha - Fe_2O_3$ [37]. The effectiveness of this process can depend on different factors like grain size [38], thermal conductivity of the irradiated region and sample preparation. This fact has to be taken into account in evaluating the impurity phases contained in the triphylite host matrix, especially for the study of relationships between the amount of magnetic clusters and the electronic conductivity of the triphylite-based materials.

5. Conclusions

In this work, through the combined use of XRPD, EPR, magnetic measurements and micro-Raman spectroscopy, we studied undoped and Mn doped $LiFePO_4$ samples obtained via solid state and sol–gel synthesis to verify the influence of synthesis route and doping on the properties of the material. The multi-technique approach allowed us to carefully characterize both the main triphylite phase and the impurity phases formed during the synthesis that, in some cases, can worsen the electrochemical properties of the material, applied as electrode in lithium batteries. By means of the complex EPR signals, magnetization curves and micro-Raman spectra, the impurity phases were identified and quantified, especially in the cases where their amount is below the detectable limit of XRPD technique. In particular, structure and amount of nano-particles clusters of maghemite were determined on the basis of magnetization results. The sol–gel synthesis seems the most suitable to obtain the undoped material for electrochemical applications, because of the lowest level of impurity phases in the sample and also the carbon coating of the triphylite particles, which can help to increase the electronic conductivity.

The Mn doped triphylite resulted in having structural, magnetic and spectroscopic features similar to the ones of the undoped sample prepared by the same synthesis route, indicating a successful substitution of Mn on the cationic sites.

The structural refinement gives new insight and interesting results concerning the Mn distribution on the cationic sites. Even though manganese preferentially substitutes for Fe^{2+} ions, the low Mn amount (about 15% of the total Mn content in the sample) present on the Li^+ site seems to be effectively responsible for the slight cell parameters and cell volume expansion observed on increasing the dopant amount. The enhanced cationic disorder induced by Mn substitution and the possible defect formation in the triphylite structure, never reported in literature to our knowledge, represent a key point in discussing the physico-chemical features of the Mn doped triphylite material. The new structural evidences should be taken into account for further work in characterizing the electrochemical behavior of the Mn doped $LiFePO_4$.

References

[1] A.K. Padhi, K.S. Nanjundaswamy, J.B. Goodenough, J. Electrochem. Soc. 144 (1997) 1188–1194.
[2] Y. Wang, J. Wang, J. Yang, Y. Nuli, Adv. Funct. Mater. 16 (2006) 2135–2140.
[3] Y. Xia, M. Yoshio, H. Noguchi, Electrochim. Acta 52 (2006) 240–245.
[4] V.A. Streltsov, E.L. Belokoneva, V.G. Tsirelson, N. Hansen, Acta Cryst. B 49 (1993) 147–153.
[5] A.S. Andersson, B. Kalska, L. Haggstrom, J.O. Thomas, Solid State Ionics 130 (2000) 41–52.
[6] C. Delacourt, C. Wurm, L. Laffont, J.B. Leriche, C. Masquelier, Solid State Ionics 177 (2006) 333–341.
[7] J. Yang, J.J. Xu, J. Electrochem. Soc. 153 (2006) A716–A723.
[8] N. Ravet, Y. Chouinard, J.F. Magnan, S. Besner, M. Gauthier, M. Armand, J. Power Sources 97 (2001) 503–507.
[9] A. Ait Salah, A. Mauger, K. Zaghib, J.B. Goodenough, N. Ravet, M. Gauthier, F. Gendron, C.M. Julien, J. Electrochem. Soc. 153 (2006) A1692–A1701.

[10] A. Caballero, M. Cruz-Yusta, J. Morales, J. Santos-Peña, E. Rodríguez-Castellón, Eur. J. Inorg. Chem. 9 (2006) 1758–1764.
[11] S.A. Needham, A. Calka, G.X. Wang, A. Mosbah, H.K. Liu, Electrochem. Commun. 8 (2006) 434–438.
[12] G.X. Wang, S. Bewlay, S.A. Needham, H.K. Liu, R.S. Liu, V.A. Drozd, J.F. Lee, J.M. Chen, J. Electrochem. Soc. 153 (2006) A25–A31.
[13] Y. Hu, M.M. Doeff, R. Kostecki, R. Finones, J. Electrochem. Soc. 151 (2004) A1279–A1285.
[14] K.-F. Hsu, S.-Y. Tsay, B.J. Hwang, J. Power Sources 146 (2005) 529–533.
[15] S.-Y. Chung, J.T. Bloking, Y.-M. Chiang, Nature Mat. 1 (2002) 123–128.
[16] A. Ait Salah, A. Mauger, C.M. Julien, F. Gendron, Mat. Sci. Eng. B 129 (2006) 232–244.
[17] M.C. Tucker, M.M. Doeff, T.J. Richardson, R. Finones, E.J. Cairns, J.A. Reimer, J. Am. Chem. Soc. 124 (2002) 3832–3833.
[18] G. Rousse, J. Rodriguez-Carvajal, S. Patoux, C. Masquelier, Chem. Mater. 15 (2003) 4082–4090.
[19] A. Goni, L. Lezama, N.O. Moreno, L. Fournes, R. Olazcuaga, G.E. Barberis, T. Rojo, Chem. Mater. 12 (2000) 62–66.
[20] K. Zaghib, A. Mauger, F. Gendron, C.M. Julien, Solid State Ionics 179 (2008) 16–23.
[21] K.-F. Hsu, S.-Y. Tsay, B.J. Hwang, J. Mater. Chem. 14 (2004) 2690–2695.
[22] Bruker AXS, TOPAS V3.0: general profile and structural analysis software for powder diffraction data. User Manual Bruker AXS, Karlsruhe, Germany, 2005.
[23] C.B. Azzoni, M.C. Mozzati, V. Massarotti, D. Capsoni, M. Bini, Solid State Sci. 9 (2007) 515–520.
[24] A. Ait Salah, J. Dodd, A. Mauger, R. Yazami, F. Gendron, C.M. Julien, Z. Anorg. Allg. Chem. 632 (2006) 1598–1605.
[25] D. Arčon, A. Zorko, R. Dominko, Z. Jagličič, J. Phys. Condens. Matter 16 (2004) 5531–5548.
[26] A. Ait Salah, K. Zaghib, A. Mauger, F. Gendron, C.M. Julien, Phys. Stat. Sol. (A) 203 (2006) R1–R3.
[27] N. Ravet, M. Gauthier, K. Zaghib, J.B. Goodenough, A. Mauger, F. Gendron, C.M. Julien, Chem. Mater. 19 (2007) 2595–2602.
[28] J. Yao, K. Konstantinov, G.X. Wang, H.K. Liu, J. Solid State Electrochem. 11 (2007) 177–185.
[29] C. Parada, J. Perles, R. Sáez-Puche, C. Ruiz-Valero, N. Snejko, Chem. Mater. 15 (2003) 3347–3351.
[30] C.M. Burba, R. Frech, J. Electrochem. Soc. 151 (2004) A1032–A1038.
[31] W. Paraguassu, P.T.C. Freire, V. Lemos, S.M. Lala, L.A. Monitoro, J.M. Rosolen, J. Raman Spectr. 36 (2005) 213–220.
[32] R.D. Shannon, Acta Cryst. A 32 (1976) 751–767.
[33] D.L.A. de Faria, S. Venaüncio Silva, M.T. de Oliveira, J. Raman Spectr. 28 (1997) 873–878.
[34] E.J. Baran, I.L. Botto, A.G. Nord, J. Molecular Structure 143 (1986) 151–154.
[35] M.M. Schieber, in: E.P. Wohlfarth (Ed.), Selected Topics in Solid State Physics, vol. 8, North-Holland, Amsterdam, 1966, p. 158 (cap. 4).
[36] K. Zaghib, A. Mauger, F. Gendron, C.M. Julien, Chem. Mater. 20 (2008) 462–469.
[37] O.N. Shebanova, P. Lazor, J. Raman Spectrosc. 34 (2003) 845–852.
[38] I.V. Chernyshova, M.F. Hochella Jr., A.S. Madden, Phys. Chem. Chem. Phys. 9 (2007) 1736–1750.